applied sciences

Article

Computer Modelling of Heliostat Fields by Ray-Tracing Techniques: Simulating Shading and Blocking Effects

José Carlos Garcia Pereira [1,*] and Luís Guerra Rosa [2]

[1] Departamento de Engenharia Química, Instituto Superior Técnico, Universidade de Lisboa, Av. Rovisco Pais, 1049-001 Lisboa, Portugal
[2] IDMEC—Instituto de Engenharia Mecânica, Instituto Superior Técnico, Universidade de Lisboa, Av. Rovisco Pais, 1049-001 Lisboa, Portugal; luisguerra@tecnico.ulisboa.pt
* Correspondence: jose.carlos.pereira@tecnico.ulisboa.pt

Featured Application: This work is directly applied to optimize the performance of heliostat fields used in solar concentrating facilities.

Abstract: In this work, solar concentrating heliostat fields are modelled using computer ray-tracing techniques to investigate the parameters controlling the optical efficiency of those solar facilities. First, it is explained how the non-trivial problem of heliostat blocking and shading can be efficiently handled in ray-tracing simulations. These numerical techniques were implemented in our Light Analysis Modelling (LAM) software, which was then used to study realistic heliostat fields for a range of different geometries. Two locations were chosen, with the highest and the lowest latitudes, from the SFERA-III EU list of solar concentrating facilities with heliostat fields: Jülich (Germany) and Protaras (Cyprus). The results indicate that shading and blocking can substantially reduce the radiation collected during the year (up to 20%). Accurate figures of merit are proposed to quantify the thermal efficiency of a heliostat field, independently of its size. Increasing the tower height mostly reduces blocking (especially when the sun is high and most energy is collected), while increasing the distance between heliostats or increasing the ground slope mostly reduces shading (especially when the sun is low and little energy is collected).

Keywords: heliostat field layout; heliostat modelling; heliostat shading and blocking; optical modelling; ray-tracing simulations

check for updates

Academic Editor: Maria Vicidomini

Received: 11 February 2025
Revised: 2 March 2025
Accepted: 7 March 2025
Published: 9 March 2025

Citation: Pereira, J.C.G.; Rosa, L.G. Computer Modelling of Heliostat Fields by Ray-Tracing Techniques: Simulating Shading and Blocking Effects. *Appl. Sci.* **2025**, *15*, 2953. https://doi.org/10.3390/app15062953

1. Introduction

In the last 50 years, a wide range of new technologies have emerged to concentrate and harness the radiation energy of the sun, such as solar furnaces (e.g., [1,2]), dish–Stirling systems (e.g., [3]), Fresnel–linear (e.g., [4]), and cylinder–parabolic concentrators (e.g., [5]), plus large heliostat fields, in some cases with many hundreds of mirrors (e.g., [6]). These technologies have always been overshadowed by non-concentrated photovoltaic (PV) solar cells, which are much easier to install and maintain. Heliostat fields still have some economic relevance in the energy sector, but all other technologies rarely make it outside research institutes. These concentrated solar power (CSP) technologies are marred by their non-trivial installation and daily operation, but also by the need to transport the thermal energy using oils or molten salts, which is always a cumbersome process.

However, CSP technologies are usually regarded as cleaner for the environment than PV, when the whole life process of its components is considered, from manufacturing to decommissioning, allowing high-energy applications that are unsuitable for PV. Computer modelling of CSP facilities can be an invaluable tool to improve the attractiveness of these technologies, allowing us to better understand and simplify its inner workings. Ray-tracing techniques in particular are ideally suited to simulate shading, blocking, and other important inefficiencies, which are easy to understand but difficult to quantify by standard methods. The more is known about these CSP facilities, the easier and cheaper it will be to use them in economic activities.

Geometric studies of shading and blocking effects in heliostat fields have recently (2019, 2022) been reported [7,8], including other attenuation contributions (such as the atmospheric attenuation used in our software). As these works show, there is no simple analytical way to solve the purely geometric problem of shading and blocking, because it depends on the many geometric parameters of the heliostats involved, plus the varying coordinates of the solar rays. Computer optimization of heliostat fields, such as the heliostat size and the aspect ratio, has also been reported (2017, 2022) using several different optimizing software approaches [9,10].

Up to now, the literature describing computer modelling of heliostat fields by ray-tracing techniques has been relatively limited. In 2009, ray-tracing software was reported by Belhomme et al. [11] at the German Aerospace Center to accurately and efficiently simulate the flux density of heliostat fields. The software was primarily designed to process real sun shape distributions and real highly resolved heliostat geometry data [11].

Later (2012), Noone et al. [12] introduced a biomimetic pattern for heliostat field layout optimization and concluded that it is possible to both reduce the land area of the plant and the number of heliostats for fixed energy collected [12]. Also in 2012, Bonanos [13] numerically examined the error sources introduced into mirror tracking systems, arising from component limitations, the construction and placement of the reflectors, and the discrete motion of the tracking system itself. He used the SolTrace software developed at the National Renewable Energy Laboratory to model CSP systems and analyze their optical performance. Commercially available ray-tracing software (like TracePro and ray-tracing Matlab code) was used by other authors [14,15] to analyze the drift of heliostats and the influence of the geometrical parameters associated with the heliostat mechanical structure and the local time.

More recent publications (2024) have also reported ray-tracing simulations aiming to optimize the working parameters in tower-type solar thermal power generation systems: (1) the simulation results allowed the authors to conclude that the average thermal power output per unit mirror area can be increased by reducing shading between the heliostats [16]; (2) the optical efficiency of the mirror field is the primary factor determining the overall system's power generation efficiency [17].

In this manuscript, computer modelling studies of heliostat fields are reported, specifically looking into the optical aspects determining their overall efficiency (in a subsequent publication, equivalent studies covering mechanical aspects will be reported).

Models are introduced to simulate the most common heliostat mirror curvatures, to handle shading, blocking, and radiation collection. Several different layouts to represent realistic heliostat fields are then suggested. Ray-tracing computer simulations of these layouts permit detecting and measuring even small optical losses due to shading and blocking effects, which are then reported and discussed. The software used was specifically written for these studies, providing maximum control, flexibility, efficiency, and accuracy, thus increasing our knowledge and our error detection capacity. This software includes the algorithms recently reported [18] to calculate the sun position (as a function of time, date, latitude, and longitude) and to simulate its non-parallel rays. Figures of merit to measure and rank the efficiency of the various heliostat fields studied, based in shading, blocking, and night effects, are then calculated and discussed.

2. Heliostat Modelling Algorithm

The overall algorithm to simulate a single heliostat is depicted in Figure 1. First, the sun position needs to be calculated for a given location and instant of time (as explained in detail in our previous work [18]). Then, the heliostat orientation must be determined, using one of the various mechanical models available. After that, the heliostat orientation needs to be transformed to the horizontal referential, to handle the simulation of the sun's rays and their reflection in the mirror, before going back to the real orientation.

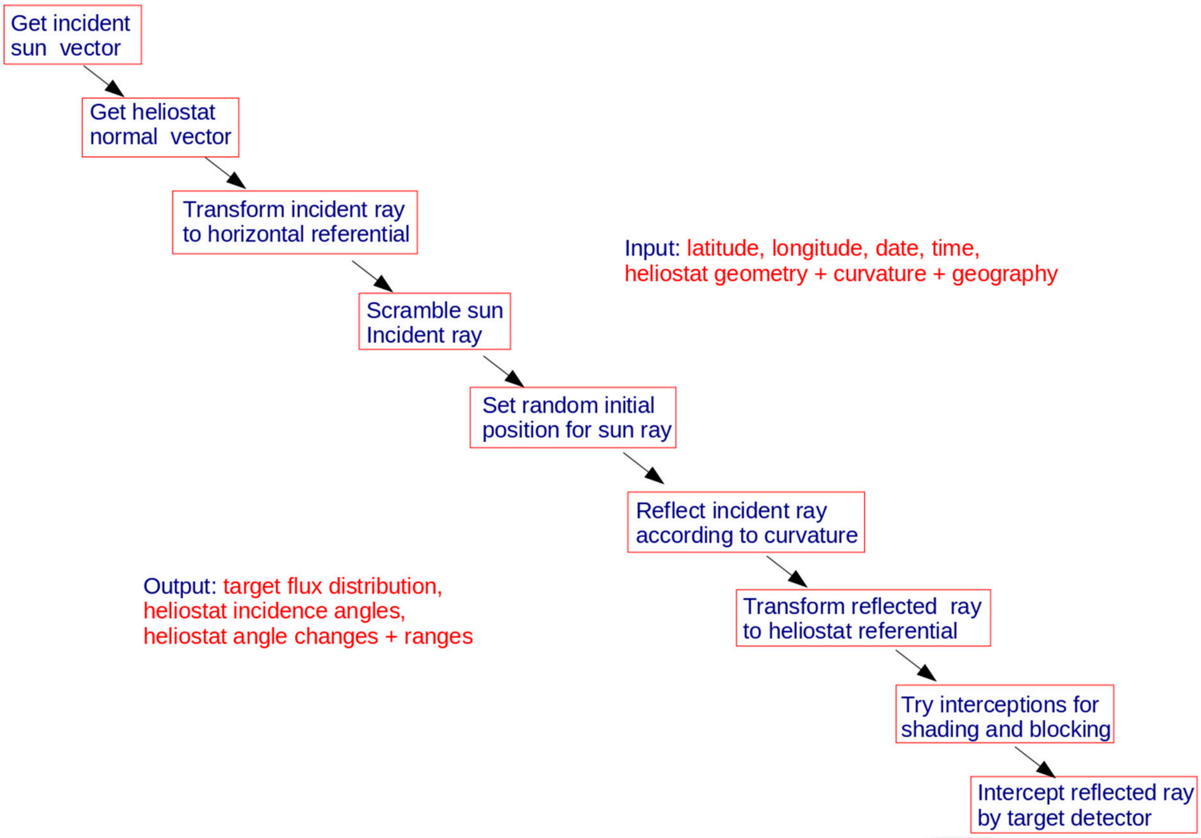

Figure 1. Overall algorithm to model a single heliostat. When modelling multiple heliostats, the geolocation data and shading/blocking attenuation effects must also be considered.

The mirror curvature plays a significant role in the way the sun's rays interact with each heliostat mirror. The heliostats are totally independent of each other, so, for example, the front-row heliostats might have a different curvature or mechanical rotation axes than the heliostats of the back row.

Then, it is necessary to check for possible shading and blocking ray interceptions, due to other neighbor heliostats in the field. Finally, the rays must be collected in the target to allow all sorts of image and data analysis. Apart from these core functionalities to simulate the heliostats at work, the software must also provide functionality to construct the heliostat field and define its mode of operation.

In our computer package, the core routines that are specifically related to heliostats amount to approximately 1900 lines of C code. This does not include, for example, image and data analysis, mathematical operations, and other general infrastructure.

3. Heliostat Curvature

Although heliostats look planar at first glance, they often have a small curvature, to help focus the light beam. It turns out that the most common curvatures, parabolic and spherical, are virtually identical for the focal lengths and heliostat dimensions required, as shown in Figure 2. As it is much easier to construct spherical rather than parabolic curvatures, most heliostats used worldwide in production or research environments are either planar (more suited for solar furnaces) or spherical (more suited for heliostat fields).

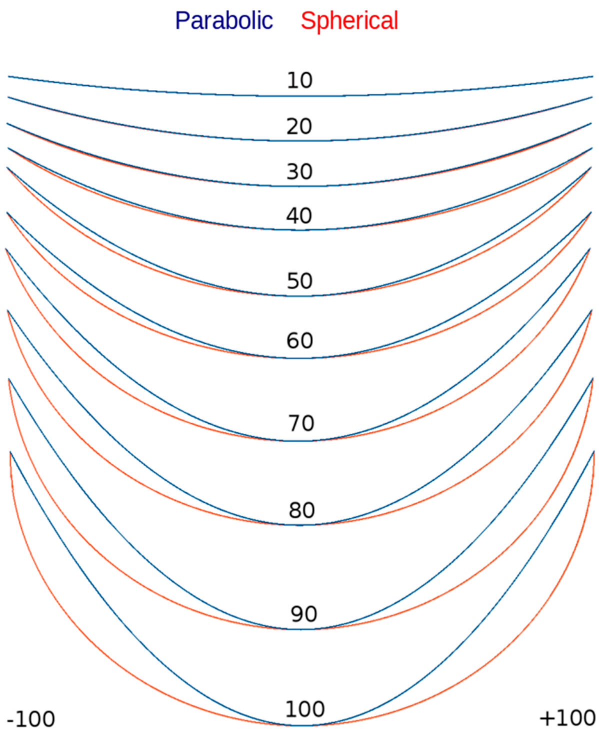

Figure 2. Comparison between parabolic (blue) and spherical (red) curvatures for a typical 200 cm × 200 cm (diagonal × diagonal) heliostat as a function of curvature deflection (all distances in cm). For deflections below 30%, parabolic and spherical curvatures are identical.

3.1. Parabolic Curvature

The focal length (f) and the curvature (a) of the paraboloid, as a function of the heliostat projected half-diagonal (x) and deflection (z), are given by the following (see Figure 3):

$$a = \frac{z}{x^2} \tag{1}$$

$$f = \frac{1}{4a} \tag{2}$$

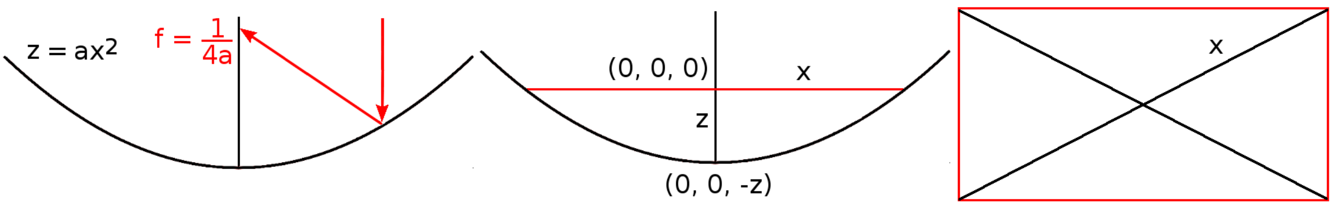

(**a**) (**b**) (**c**)

Figure 3. (**a**) Paraboloid curvature a and focal length f (see [19] for details) are functions of heliostat deflection z shown in (**b**) and heliostat projected half-diagonal x depicted in (**c**). Random reflection points and incident sun rays are generated in the rectangle (in red) at height 0 (lateral and top views) before intercepting the heliostat curvature (in black) below, where the reflection actually occurs.

3.2. Spherical Curvature

The focal length (f) and the radius of the sphere (r), as a function of the heliostat projected half-diagonal (x) and deflection (z), are given by the following (see Figure 4):

$$(r-z)^2 + x^2 = r^2 \quad \Rightarrow \quad r = \frac{z}{2} + \frac{x^2}{2z} \tag{3}$$

$$\alpha_{max} = \arcsin\frac{x}{r} \tag{4}$$

$$f = r - \frac{r}{2\cos\alpha} \tag{5}$$

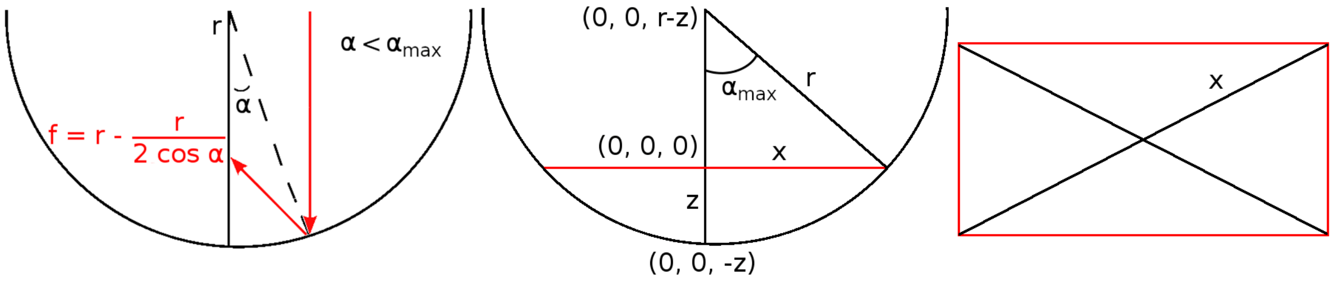

Figure 4. (**a**) Spherical radius r and focal length f (see [19] for details) are functions of heliostat deflection z shown in (**b**) and heliostat projected half-diagonal x depicted in (**c**). Random reflection points and incident sun rays are generated in the rectangle (in red) at height 0 (lateral and top views) before intercepting the heliostat curvature (in black) below, where the reflection actually occurs.

Unlike a parabolic curvature, the focal length in a spherical curvature is not constant and depends on the angle α (see Figure 4). The maximum focal length f_{max} occurs in the center, where $\alpha = 0°$ and $f_{max} = \frac{r}{2}$. The minimum focal length f_{min} occurs at the border, where $\alpha = \alpha_{max}$. When $\alpha_{max} > 60°$, f_{min} becomes negative, because the parallel ray is reflected again before reaching the spherical axis.

In heliostat fields, typical focal distances (f) are usually between 25 m and 250 m (spherical radius between 50 m and 500 m). As shown in Table 1 for a typical 200 cm × 200 cm (diagonal × diagonal) heliostat, those values correspond to deflections z between 1 cm (1%) and 0.1 cm (0.1%), and rim angles α_{max} (see Figure 4) between 1.15° and 0.11°.

In our ray-tracing model, random points (simulating the points where the sun rays are reflected) are generated in a horizontal rectangle representing the projected heliostat. For each reflection point, a sun ray is generated, using the astronomical algorithm and random scrambling transformations described elsewhere [18]. Each reflection point and sun vector is then used to calculate the ray interception and corresponding normal vector with the curved surface, immediately below the rectangle. How to analytically calculate the ray interception with a parabolic or spherical surface, the corresponding normal vector, and output reflected vector is discussed in our previous work [19,20].

Table 1. Parabolic focal length f, maximum f_{max} ($\alpha = 0°$) and minimum f_{min} ($\alpha = \alpha_{max}$) spherical focal length, plus spherical rim angle α_{max}, as a function of heliostat deflection z in a 200 cm × 200 cm (diagonal × diagonal) heliostat.

z (cm)	f (cm)	f_{max} (cm)	f_{min} (cm)	α_{max}
0.1	25,000.0	25,000.0	25,000.0	0.11°
0.5	5000.0	5000.1	4999.9	0.57°
1.0	2500.0	2500.3	2499.7	1.15°
5.0	500.0	501.3	498.7	5.7°
10.0	250.0	252.5	247.4	11.4°
20.0	125.0	130.0	119.2	22.6°
30.0	83.3	90.8	72.9	33.4°
40.0	62.5	72.5	44.9	43.6°
50.0	50.0	62.5	20.8	53.1°
60.0	41.7	56.7		61.9°
70.0	35.7	53.2		70.0°
80.0	31.3	51.3		77.3°
90.0	27.8	50.3		84.0°
100.0	25.0	50.0		90.0°

Note: For common heliostats, 25 m < f < 250 m. As $z \to 0$, $\alpha_{max} \to 0$ and $f \approx f_{min} \approx f_{max} = \frac{r}{2}$.

4. Light Attenuation

There are several mechanisms that contribute to reducing the radiation that reaches the target. For most studies of heliostat fields at work, involving geometric parameters or comparisons between different situations, these attenuation effects can usually be ignored (implicitly assuming that they affect the various situations equally). However, to estimate the flux of energy collected in the target, these effects should be taken into account. Shading and blocking simulations are important to optimize the heliostat field layout, maximizing land use without causing obstructions between heliostats.

4.1. Shading/Blocking

Shading occurs when radiation coming from the sun that should illuminate the heliostat mirror is obstructed before by some other heliostat. Blocking occurs when radiation reflected by the heliostat mirror is obstructed by some other heliostat before reaching the target (see Figure 5). These effects (see for example [7,8]) may occur when the heliostats are too close or when the target is too low. The sun being at low altitude (in winter and at dawn and dusk) contributes significantly to these effects. Clearly, they should not play a major role in well-designed heliostat fields collecting thermal energy.

Fortunately, shading and blocking can be easily simulated in an elegant, robust way in ray-tracing software. For each generated reflection point in the heliostat surface, there is an input wave vector coming from the sun and an output wave vector pointing to the target. If the line defined by the input wave vector intercepts any other heliostat, a shading event occurs, and this ray is lost. If the line defined by the output wave vector intercepts any other heliostat, a blocking event occurs, and this ray is lost. To find out whether a ray intercepts some other heliostat:

(1) Use the four vertices defining the rectangle polygon of each neighbor heliostat to calculate its center and normal vector (see Figure 6). The neighbor heliostats can be in the rest position, sun-orientated, or in any other arbitrary orientation defined by the rotating angles α and β, with varying results.

(2) Determine the ray interception with the neighbor heliostat plane (see [19,20] for details).

(3) Check whether the interception point is inside or outside the neighbor heliostat polygon (see Figure 7). When the point is inside, the cross product of successive vectors from the polygon center to the polygon vertices always points to the same polygon side, so the dot product of these cross vectors is always positive. When the point is outside, some of the cross products will produce vectors in opposite directions, so at least one of the dot products of these cross vectors will be negative (our group has used this technique extensively in the past to study the behavior of homogenizers in high-flux solar furnaces [21]).

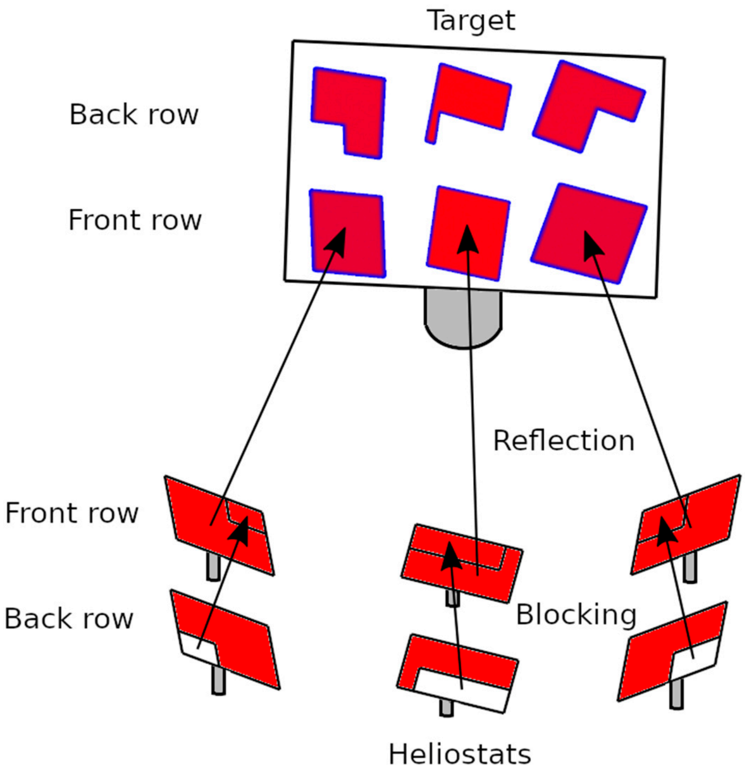

Figure 5. Radiation accumulated at the target of a 3 × 2 heliostat field (simulated with 10^8 rays), showing heliostat blocking: the three back-row heliostats (pointing above) are partly blocked by the three front-row heliostats (pointing below). In this example, the target is 6 m higher than the 2 m × 2 m heliostats, which are 2 m apart.

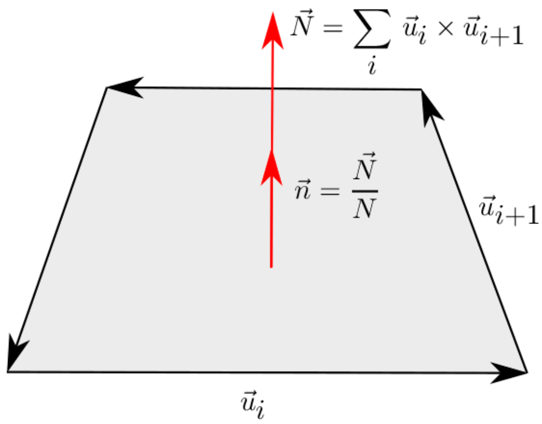

Figure 6. Adding the cross products between successive edge vectors is an effective way to calculate the normal vector of a convex, flat polygon.

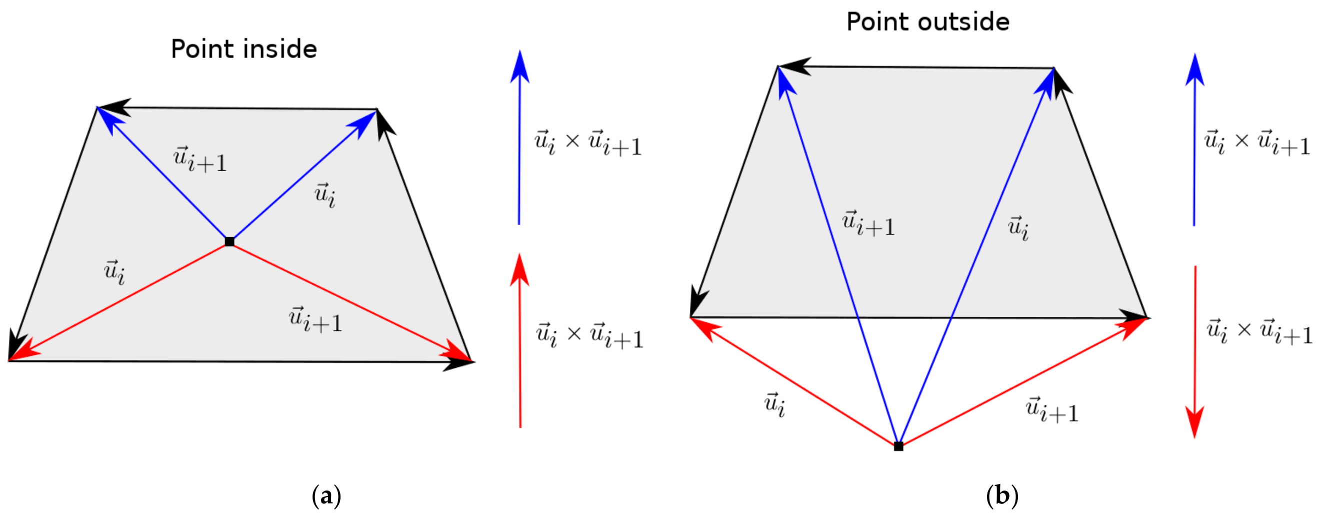

Figure 7. The successive cross product vectors always point (**a**) to the same side (inside point) or (**b**) to opposite sides (outside point), permitting us to distinguish between the two situations.

4.2. Mechanical Collisions

The software also tests for mechanical collisions between the heliostat mirrors or with the ground. For each mirror vertex with x,y,z coordinates, the z coordinate is compared with the soil z coordinate for that x,y location. Each heliostat mirror can be represented by a sphere, with a radius going from the center to a vertex. If this sphere intercepts the sphere of a neighbor mirror, a collision occurs. Unlike shading and blocking, which need to be tested only after each heliostat alignment, mechanical collisions must be tested throughout the mechanical rotation process (fortunately, this is a quick test).

4.3. Atmospheric Attenuation

According to several authors (e.g., [12,22,23]), the radiation attenuation due to atmospheric effects occurring between the heliostats and the target can be tentatively described using the following equations:

$$D \leq 1000 \text{ m:} \qquad \eta_{atm} = 0.99321 - 0.0001176D + 1.97 \times 10^{-8} D^2 \tag{6}$$

$$D \leq 1000 \text{ m:} \qquad \eta_{atm} = \exp(-0.0001106D) \tag{7}$$

where D is the distance between the mirror center and the collecting target (D is actually implemented in the source code as the distance between the reflection point in the heliostat and the collecting target).

4.4. Angle Attenuation

The cosine efficiency measures the loss of radiation (energy) due to radiation absorption and scattering effects resulting from the angle between the heliostat normal vector (n) and the incident sun ray (s) [24]:

$$\eta_{cos} = \frac{\vec{n} \cdot \vec{s}}{|n||s|} \tag{8}$$

4.5. Reflectivity Attenuation

The experimental reflectivity of a good mirror in the UV–visible–near-infrared range is usually between 0.85 and 0.95. In these simulations, a conservative approach has been adopted, using the lowest value (to account for dust, moisture, corrosion, wind, etc.):

$$\eta_{ref} \approx 0.85 \tag{9}$$

The overall light attenuation can then be estimated for each simulated ray, multiplying the above attenuation factors:

$$\eta = \eta_{atm}\,\eta_{cos}\ \ \eta_{ref} \tag{10}$$

Other effects, such as interception efficiency (see [7]), are currently not considered in our software.

5. Light Collection

To collect light rays intercepting the target, a pixel-based rectangle is used, characterized by position, normal, and up vectors (like a photographic camera). Ideally, the target plane may be orientated to be normal to the average direction of the rays coming from the heliostat field (see Figure 8). Large energy production heliostat fields tend to have a central tower collecting the sun radiation, so the target can be simulated by a ray intercepting cylinder, which is then unwrapped after collecting the rays to produce a planar, pixel-based rectangle, as before. The data acquired can then be used to produce images, statistical data, profiles, etc. (this is extensively illustrated in our previous works [19–21]).

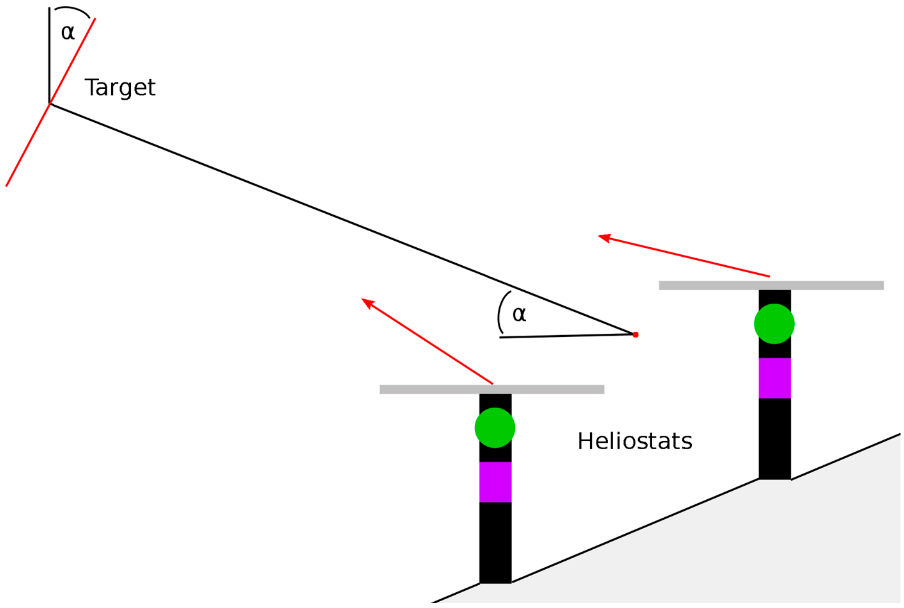

Figure 8. Pixel-based target rectangle, perpendicular to average sun radiation coming from the heliostat field (heliostats are represented in the rest position).

6. Computational Details

Unless we are studying an already-existing heliostat field, many choices and compromises must be taken into account before designing the new model:

(1) How many heliostats shall we model? In a computer with an i5 processor, each heliostat ray-tracing simulation takes 1 min of CPU time for 10^8 rays. Therefore, the number of heliostats should be kept to a minimum. To simulate a heliostat field close to reality, we used the layout shown in Figure 9, with a total of 66 heliostats in a staggered arrangement. However, only the six end heliostats (in green) are fully simulated as we identify them as representatives of the whole set. The 20 first neighbors (in red) and the 8 s neighbors (in pink) must also be orientated to catch possible blocking and shading events (but this task does not involve ray tracing, so it is not time-consuming). We assume that only these first and second neighbor heliostats can effectively contribute to shading or blocking events. This is possible because blocking events are due to close heliostats only (the reflected rays must travel upwards to the target) and shading events can be seen as resulting from close

heliostats only (even when the received rays are almost horizontal, close heliostats will stop most rays stopped by farther heliostats). During this work, we will be independently simulating each of these six groups of heliostats (henceforth named N, NW, NE, S, SW, and SE, as shown in Figure 9), formed by one green heliostat, three or four red heliostats, and one or two pink heliostats.

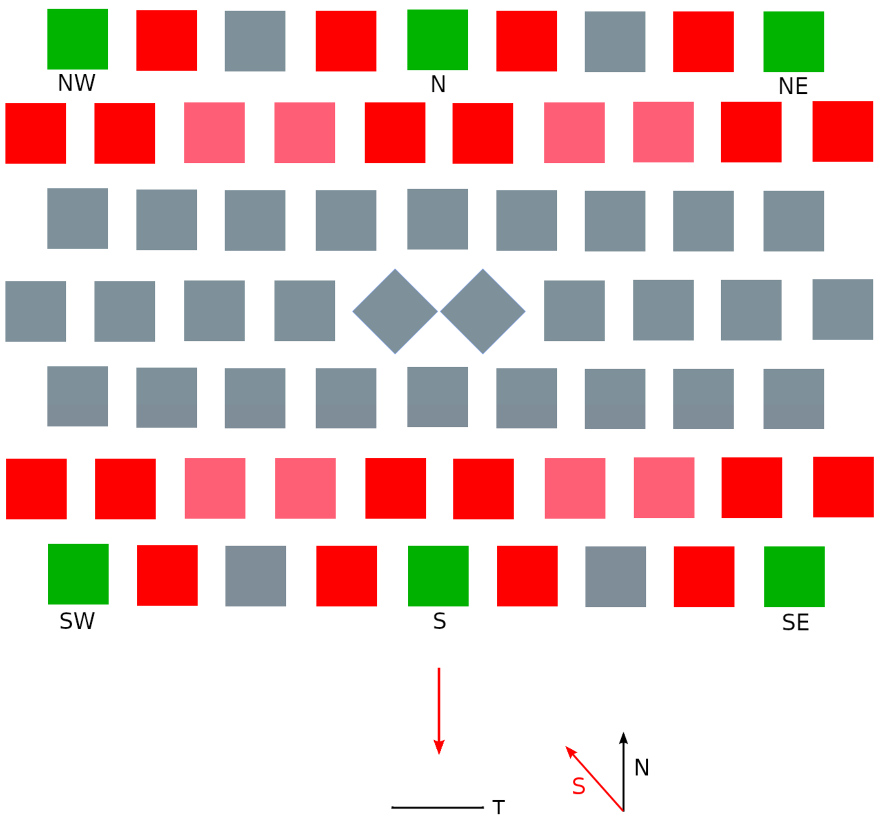

Figure 9. Layout for the simulated heliostat field, with 66 heliostats in a staggered arrangement. The target (T) points north (N), to collect the sun rays (S) reflected. Only the 6 green heliostats are fully simulated. The 20 closer (red) and 8 farther (pink) heliostats must be orientated, to test for possible blocking and shading events. The heliostat mirrors are 2.0 m × 2.0 m, separated by 1.0 m in both the north–south and east–west directions. The two central heliostats are rotated 45° to emphasize that they cannot touch. We also simulated this heliostat field with mirrors 2.5 m (east–west) × 1.6 m (north–south), with 1.0 m separation east–west and 1.9 m north–south.

(2) Shall we simulate a horizontal field or a field making some south–north slope angle? If so, should it be 10° or 20°? Using a slope is more interesting, but choosing a horizontal flat terrain is simpler, on average closer to real land conditions, and better emphasizes the differences between the front and the back heliostat rows. In this work, we simulate and compare the 0° and 10° slopes.

(3) Shall we use square or rectangular heliostats? And which dimensions shall we use? Larger sizes provide larger radiant energy but are less flexible to handle and require stronger mechanical structures to cope with the wind. Rectangular heliostats might handle wind better than square heliostats with the same area, due to their lower height. In this work, we use heliostats with an area of 4 m^2 each. We compare square 2.0 m × 2.0 m with rectangular (5/2) × (2/5 × 4) = 2.5 m × 1.6 m heliostats (typical sizes in tilt–roll heliostat fields). Therefore, the total power of our heliostat model (assuming an average DNI = 800 W/m^2) becomes 66 × 4 × 800 = 0.21 MW.

(4) What should the distance between the heliostat mirrors be in the resting, flat position? Land is expensive, so heliostats should be kept as close as possible, to maximize

the collected power, but not closer, to avoid blocking and shading events and mechanical collisions [25]. In square heliostats, we choose 1.0 m for both east–west and north–south separation. In rectangular heliostats, we choose the same 1.0 m for east–west separation and 1.9 m (2.5 + 1.0 − 1.6) for north–south separation (so the same 1.0 m separation is obtained if the heliostats are rotated 90°). In our simulations, we also check if the four mirror vertices are touching the ground or neighboring mirrors.

(5) For the 66-heliostat field just proposed, where shall the target be positioned to avoid significant blocking/shading effects? We choose to initially position the target 15 m high, 10 m away from the center of the closer row of heliostats, similar to the target built for the IMDEA Energy heliostat field at the Technology Park of Móstoles, Spain [26]. Simulating afterwards the radiation received throughout the year (particularly in winter), we can acquire insightful information and make adjustments to the target position accordingly.

(6) Assuming that we choose a spherical curvature for the heliostats, what should the deflection be (2 cm, 1 cm, or 0.5 cm)? The actual choice depends on the average distance from the heliostats to the target, which in our case ranges from 21.3 m (square heliostats, 10° slope) to 24.3 m (rectangular heliostats, no slope). For example, in the 169-heliostat field of IMDEA, Madrid, two different curvatures were used, for heliostats closer to and farther from the target [12]. In our case, for the 2.0 m × 2.0 m square heliostats, the focal distance is 24.8 m for 2.0 cm and 49.7 m for 1.0 cm, while for the 2.5 m × 1.6 m rectangular heliostats, the focal distance is 27.4 m for 2.0 cm and 54.8 m for 1.0 cm. For the sake of simplicity, we choose to use the same deflection for all heliostats (so closer heliostats produce larger, less concentrated target images). We choose 1.0 cm for deflection, as we do not want to focus the radiation at the target, only to slightly concentrate the radiation. (We do not want to melt the target!)

(7) Finally, we need to set the location of the heliostat field, as the latitude plays a significant role in determining the sun's trajectory over the local site throughout the year. For this work, we selected the two locations with higher and lower latitude from the list reported by SFERA-III [27] for European Union CSP research infrastructures with heliostat fields: Jülich, Germany (latitude = 50.9133°, longitude = 6.3878°), and Protaras, Cyprus (latitude = 35.0125°, longitude = 34.0583°). This 15° difference in latitude between the two locations is enough to produce insightful changes between the two sets of results.

A second group of choices must also be considered regarding working conditions:

(i) It seems logical to scan a full year, from 1st January to 31st December, for instance 2024. But what should the scanning frequency be? Every hour seems a good compromise, to detect blocking and shading events, as the danger of losing significant events seems small, and the needed computing time is not impossibly high (for this particular task, using 10^6 rays is acceptable, as we are not attempting to create a very accurate image of the radiation on the target; we are only checking for interception events). To obtain an accurate measurement of the total mechanical rotations made and the maximum mechanical angles achieved, every minute or every 5 min is probably needed (no time-consuming ray tracing is involved, as we only need to orientate the heliostats).

(ii) What is the daily working range? We choose the range of 08:00 to 16:00 LCT time (i.e., local time). This depends on the date and latitude, but for most common places, it seems a reasonable choice. We note that throughout this work, we ignore daylight saving time (DST) and other purely administrative or political changes to standard local time.

(iii) The heliostats should start every day from the flat resting position and come back to this position at the end of the day (mostly to protect the heliostats from strong winds during the night). This seems the most reasonable option, but it increases the rotations that the heliostats must perform.

(iv) For research purposes, we want to point each heliostat at a different region of the target (as in Figure 5), so we can study each heliostat's results separately. Therefore, we used a large 9 m × 5 m target, with horizontal and vertical separation between heliostat images of 3.0 m and 2.0 m, respectively.

Our computational simulations were implemented using our Light Analysis Modelling (LAM) software. This is a small, purely academic project that we have been developing since 2017 to fulfill our own needs, covering different subjects, from solar furnaces to optical lenses. It is very efficient, written in C, with all the reflections and refractions handled in a purely analytical way, with the code distributed over 15 files, containing about 9000 lines of source code.

7. Results and Discussion

Each of the six representative heliostats, with its corresponding group (SW, S, SE, NW, N, or NE), was simulated independently for each of the eight configurations studied in this work: Jülich (J) or Protaras (P) locations, rectangular (R) or square (S) heliostats, and flat (F) or sloped (S) ground. This produces 48 files describing all the obstacle events (night-time, fraction of rays stopped by shading, and fraction of rays stopped by blocking) for all the nine sampling times, starting at 08:00 up to 16:00 LCT time, covering the whole 8 h working range for all 366 days (leap year) in 2024. All results reported here (including Figures 10–17 and Tables 2–4) were obtained using our software, with the working parameters discussed in Section 6 (Computational Details).

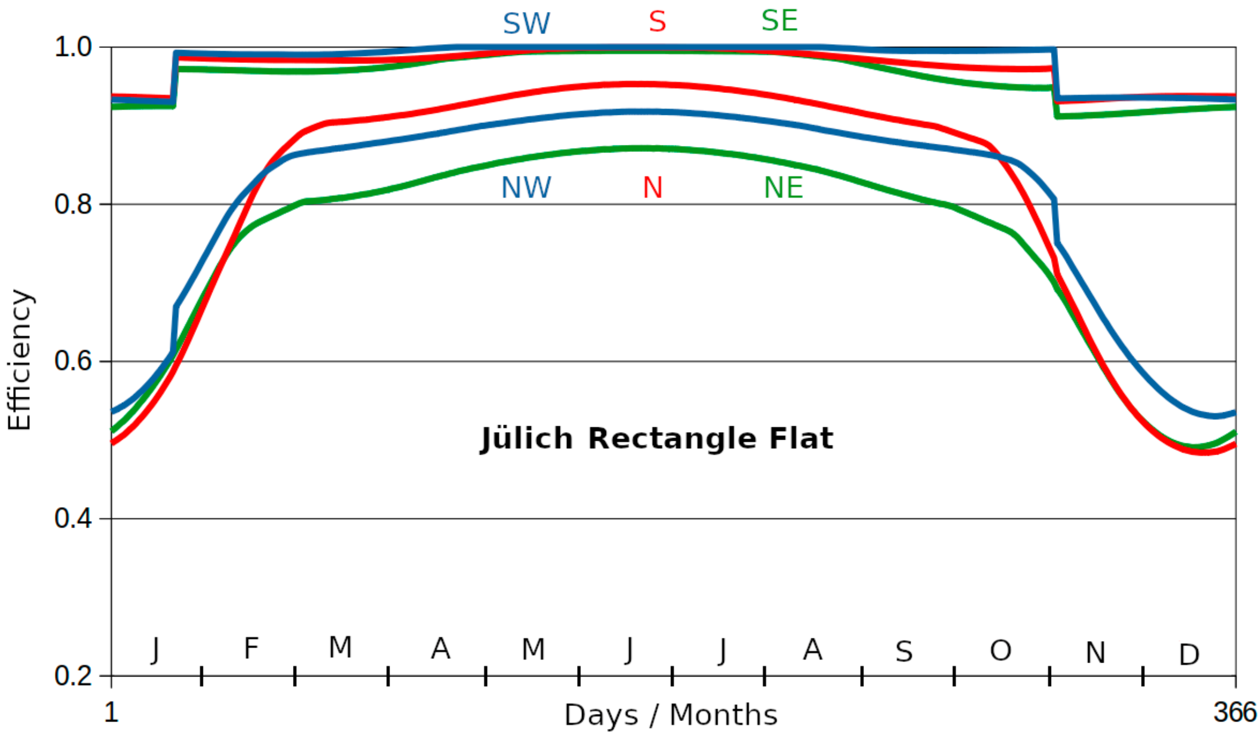

Figure 10. Daily heliostat efficiency (DHE) calculated for SW, S, SE, NW, N, and NE representative heliostats (see Figure 9), for Jülich, with rectangular heliostats and flat ground (from 3rd November to 21st January, it is night at 16:00 LCT).

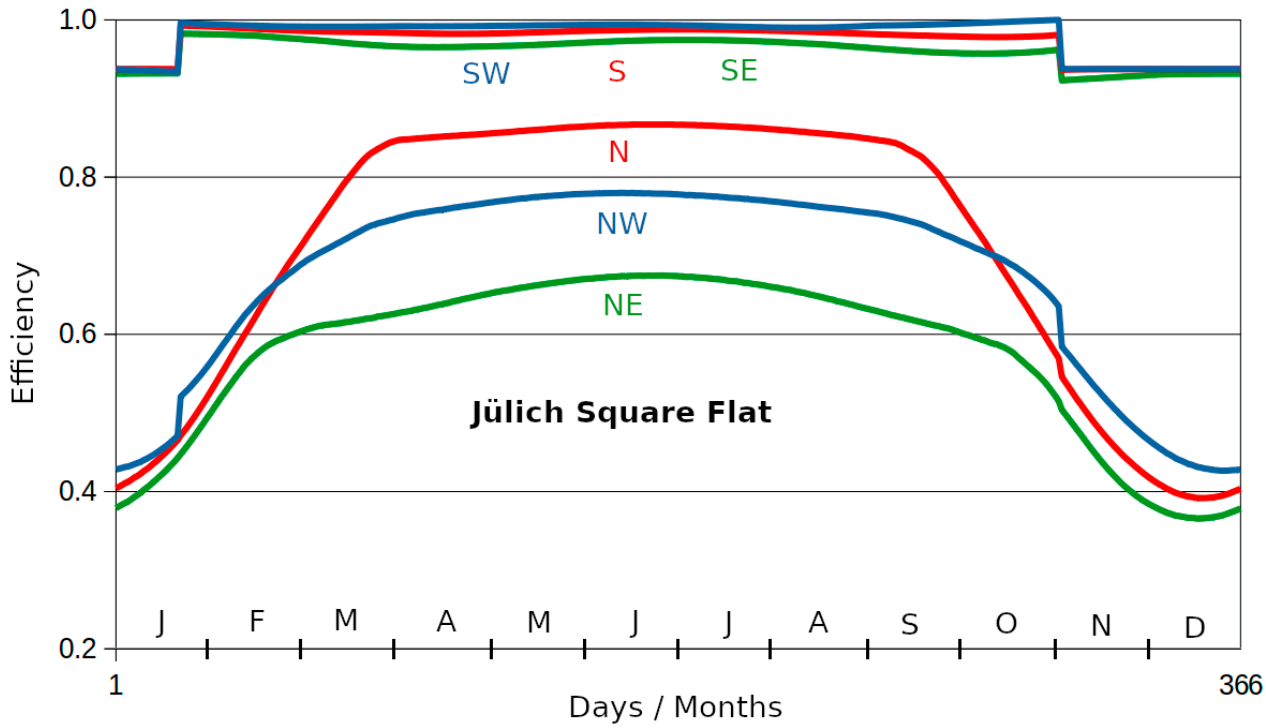

Figure 11. Daily heliostat efficiency (DHE) calculated for SW, S, SE, NW, N, and NE representative heliostats (see Figure 9), for Jülich, with square heliostats and flat ground (from 3rd November to 21st January, it is night at 16:00 LCT).

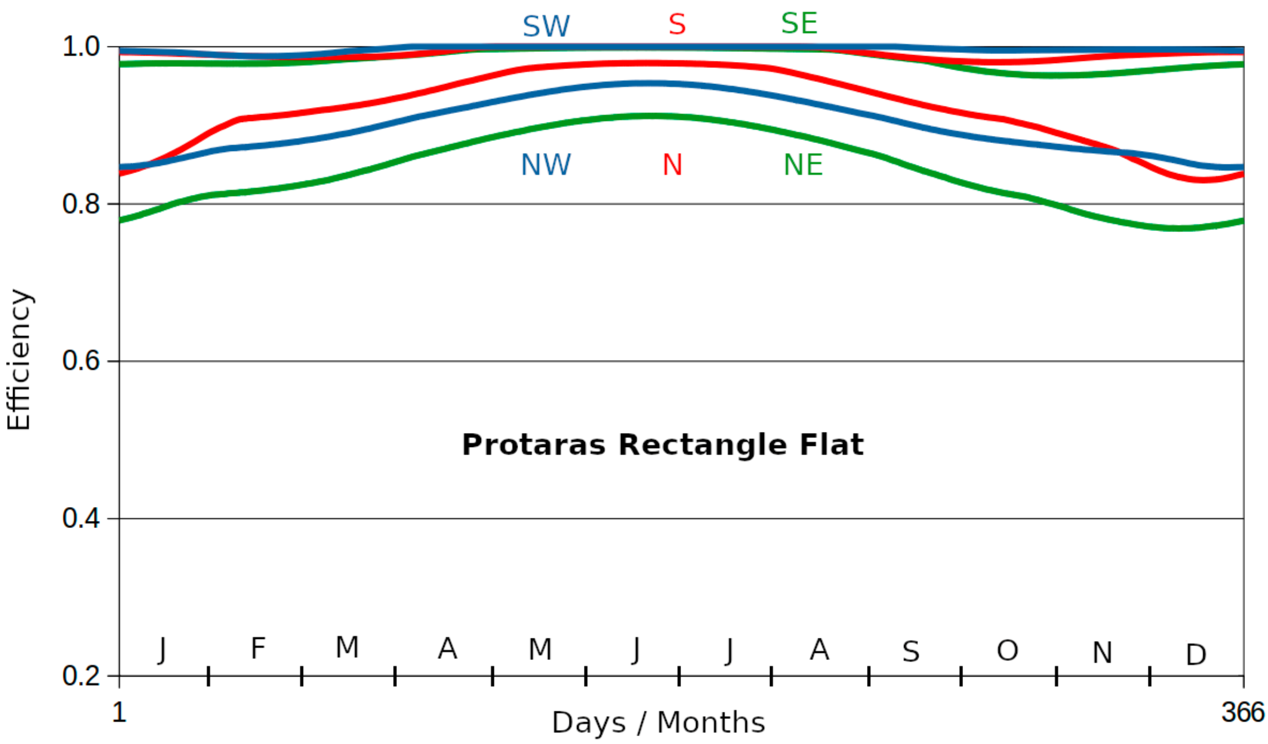

Figure 12. Daily heliostat efficiency (DHE) calculated for SW, S, SE, NW, N, and NE representative heliostats (see Figure 9), for Protaras, with rectangular heliostats and flat ground.

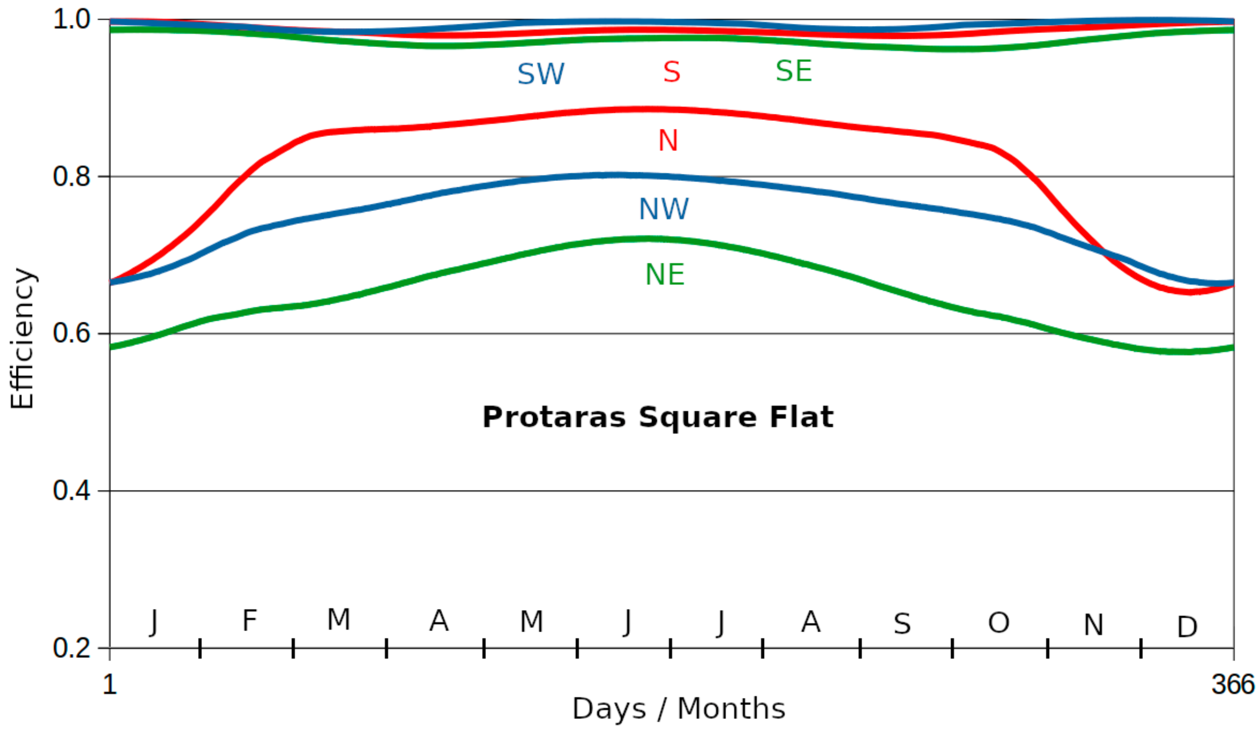

Figure 13. Daily heliostat efficiency (DHE) calculated for SW, S, SE, NW, N, and NE representative heliostats (see Figure 9), for Protaras, with square heliostats and flat ground.

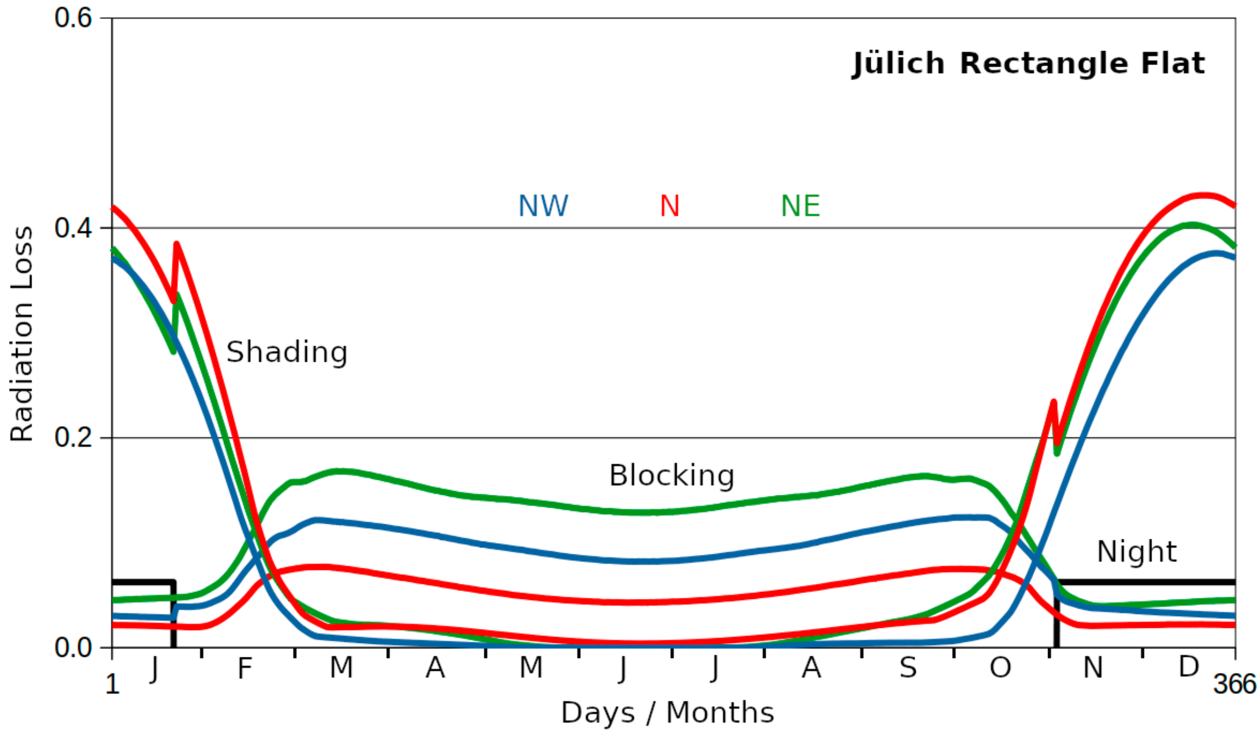

Figure 14. Radiation loss (night, shading, and blocking effects) calculated for NW, N, and NE representative heliostats (see Figure 9), for Jülich, with rectangular heliostats and flat ground (from 3rd November to 21st January, it is night at 16:00 LCT).

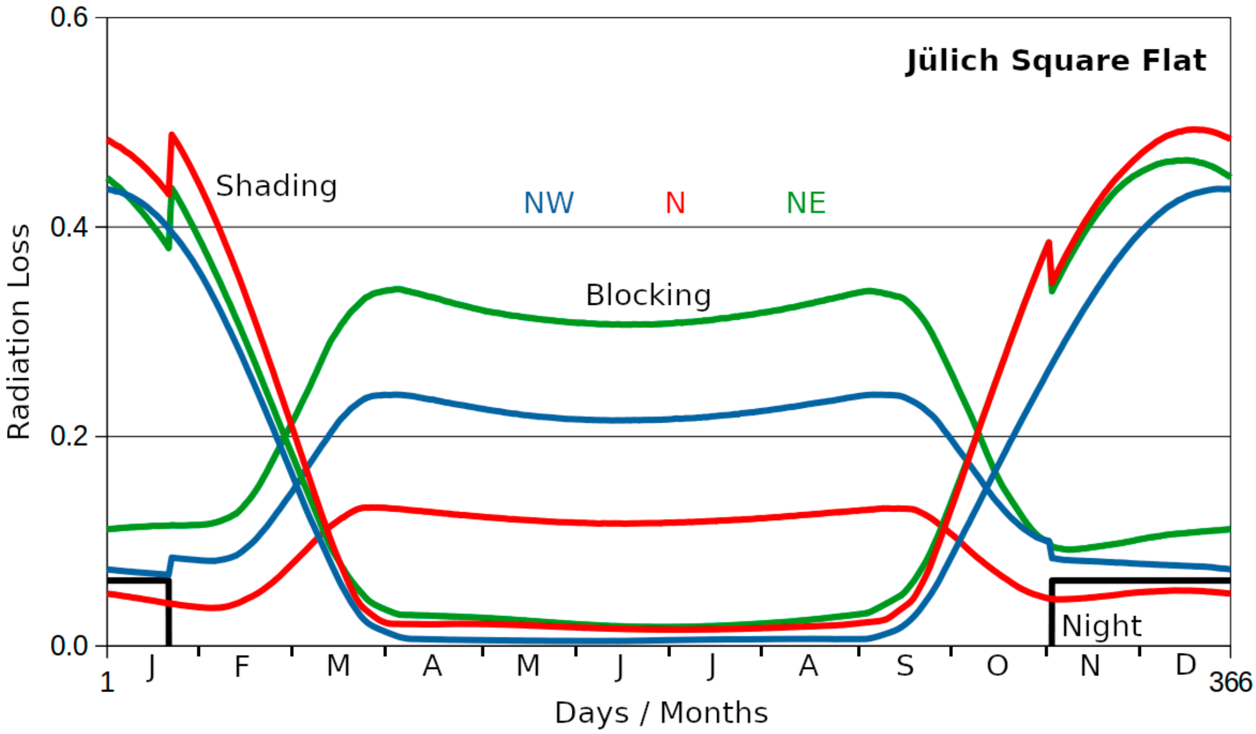

Figure 15. Radiation loss (night, shading, and blocking effects) calculated for NW, N, and NE representative heliostats (see Figure 9), for Jülich, with square heliostats and flat ground (from 3rd November to 21st January, it is night at 16:00 LCT).

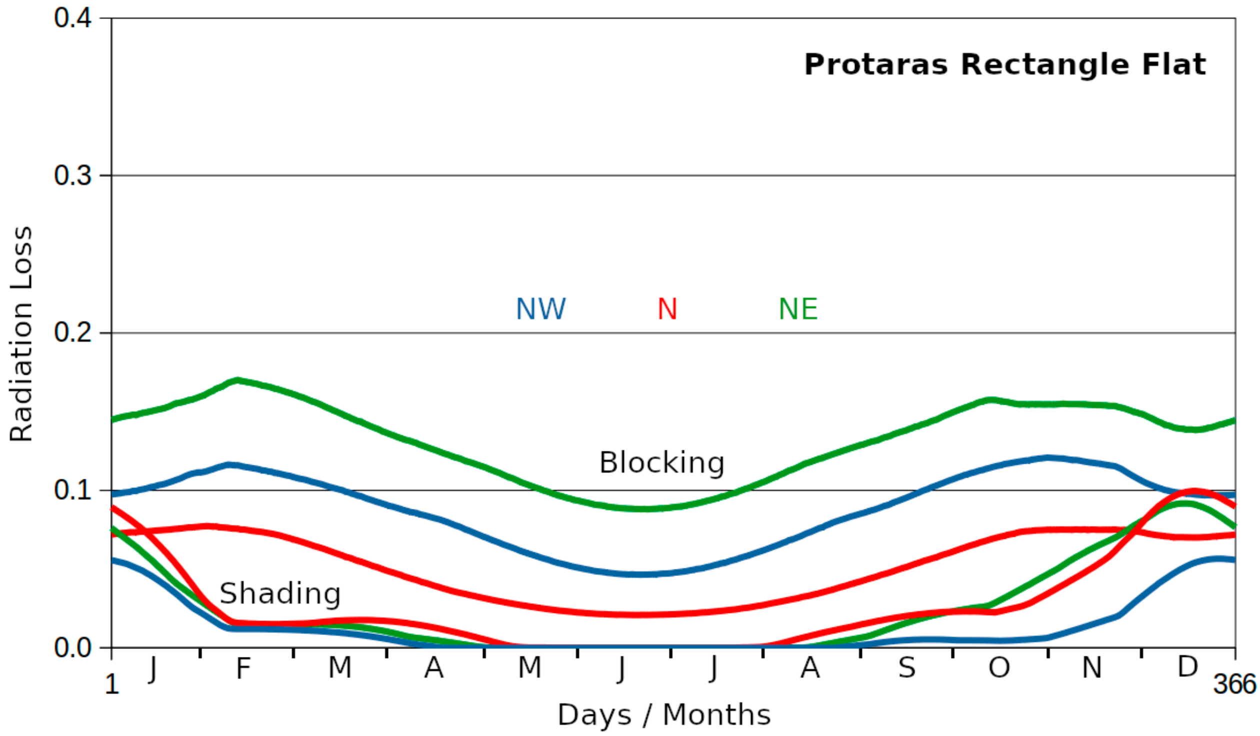

Figure 16. Radiation loss (shading and blocking effects) calculated for NW, N, and NE representative heliostats (see Figure 9), for Protaras, with rectangle heliostats and flat ground.

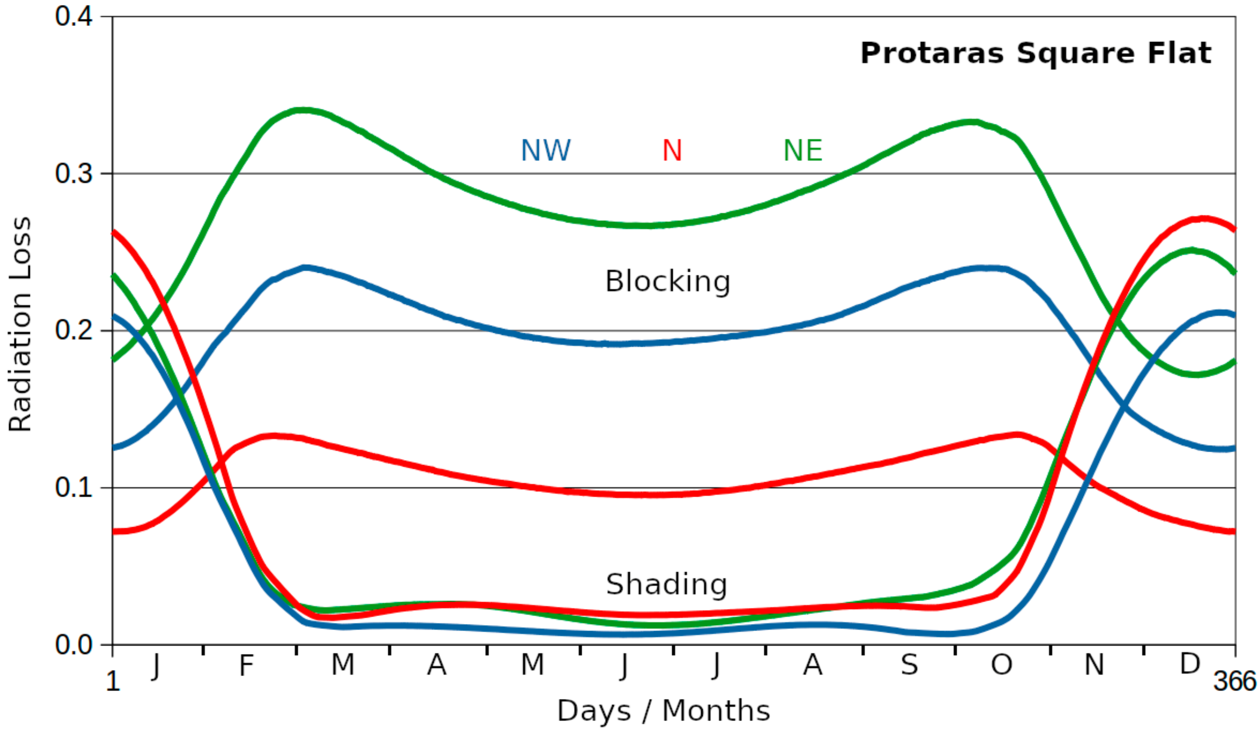

Figure 17. Radiation loss (shading and blocking effects) calculated for NW, N, and NE representative heliostats (see Figure 9), for Protaras, with square heliostats and flat ground.

Table 2. YHE and average (AHE) for the 8 configurations, Jülich (J) or Protaras (P) location, rectangular (R) or square (S) heliostats, and flat (F) or sloped (S) ground for SW, S, SE, NW, N, and NE heliostats.

	SW	S	SE	NW	N	NE	AHE
JRF	0.9830	0.9763	0.9658	0.8141	0.8176	0.7592	0.8213
JRS	0.9829	0.9763	0.9572	0.8985	0.9051	0.8581	0.8988
JSF	0.9808	0.9742	0.9605	0.6729	0.7118	0.5754	0.6968
JSS	0.9807	0.9748	0.9571	0.7398	0.7911	0.6496	0.7601
PRF	0.9968	0.9921	0.9845	0.9000	0.9223	0.8438	0.9027
PRS	0.9967	0.9920	0.9764	0.9424	0.9548	0.9094	0.9427
PSF	0.9927	0.9862	0.9737	0.7498	0.8157	0.6506	0.7722
PSS	0.9925	0.9865	0.9698	0.7910	0.8625	0.7019	0.8121

Table 3. YTE and average (ATE) for the 8 configurations, Jülich (J) or Protaras (P), rectangles (R) or squares (S), and flat (F) or slope (S), for SW, S, SE, NW, N, and NE heliostats.

	SW	S	SE	NW	N	NE	ATE
JRF	0.4234	0.4219	0.4187	0.3701	0.3795	0.3490	0.3737
JRS	0.4234	0.4218	0.4149	0.3955	0.4008	0.3812	0.3963
JSF	0.4219	0.4204	0.4156	0.3072	0.3372	0.2658	0.3192
JSS	0.4219	0.4206	0.4142	0.3279	0.3581	0.2901	0.3381
PRF	0.5491	0.5480	0.5449	0.5025	0.5159	0.4752	0.5046
PRS	0.5491	0.5480	0.5403	0.5252	0.5309	0.5107	0.5255
PSF	0.5469	0.5449	0.5393	0.4180	0.4616	0.3667	0.4329
PSS	0.5469	0.5449	0.5371	0.4396	0.4807	0.3949	0.4526

Table 4. AHE and ATE for improved configurations: JSF_1 (JSF with heliostat distance of 2 m), JSF_2 (JSF with tower height of 20 m), JSF_3 (JSF with slope of 20°), and PRS_{123} (PRS with the three previous improvements combined). Results for the original configurations (JSF and PRS) can be seen in Table 2 (AHE) and Table 3 (ATE).

	JSF_1	JSF_2	JSF_3	PRS_{123}
AHE	0.8052	0.7822	0.7985	0.9989
ATE	0.3600	0.3625	0.3501	0.5498

7.1. Daily Heliostat Efficiency (DHE)

To start integrating all these data, an hourly heliostat efficiency (HHE) can be defined:

$$\mathrm{HHE} = 1 - S - B \tag{11}$$

where S and B represent the fraction of shading and blocking occurring at that hour. When the altitude is negative (night-time), HHE = 0. This quantity in turn can be used to define a daily heliostat efficiency (DHE):

$$\mathrm{DHE} = \frac{0.5\mathrm{HHE}_8 + \sum_{i=9}^{15} \mathrm{HHE}_i + 0.5\mathrm{HHE}_{16}}{8} \tag{12}$$

DHE can be plotted over the year, as shown in Figures 10–13, for Jülich and Protaras and for rectangular and square heliostat configurations. Each figure shows independent curves for the six representative heliostats (colored green in Figure 9) simulated in our work.

In all four of these configurations, efficiency is close to 1.0 for the front-row heliostats (SW, S, and SE) but drops significantly for the other heliostats, even in summer, due to shading/blocking events. This was expected because front heliostats cannot be blocked and can only suffer some east–west shading, mainly in spring and autumn, when the sun's azimuth is closer to the east (90°) or west (270°), because in winter, the sun comes more from south (the azimuth is closer to 180°).

Clearly, the three back heliostats (NW, N, and NE) seem to be much more representative of the average heliostat functionality for the whole field than the front heliostats. Comparing only the three back heliostats, for all four configurations shown here, the NE heliostat has the lowest efficiency, and the N heliostat has the highest. This happens because the sun altitude in Jülich and Protaras is always higher at 08:00 than at 16:00 LCT, as these locations are in the easterly side of the time zone. The NE heliostat cannot be shaded at 8 h (clear view to the sun) but is significantly shaded at 16 h. The NW heliostat is shaded at 8 h but not at 16 h (clear view to the sun), so the NW efficiency is better than for NE. The central N heliostat is geometrically closer to the target than the corner NW and NE heliostats, so the ray angles from the N heliostat to the target are substantially higher, thus reducing blocking events.

As expected, efficiency losses are much higher in Jülich than in Protaras, particularly in winter, as the altitude of sun trajectories decreases rapidly with latitude, resulting in more shading events.

In Jülich and Protaras, efficiency is much higher for rectangular than for square heliostats. This happens because our square heliostats are taller (2.0 m) than the rectangular heliostats (1.6 m) with the same area (4 m^2), making the occurrence of blocking events in the upper part of front heliostats more probable. Moreover, to guarantee that heliostat mirrors are 1.0 m apart, even when rotated 90°, the north–south distance between the rectangular heliostats is larger (1.90 m) than in square heliostats (1.0 m), thus increasing the space around each heliostat and decreasing the probability of shading/blocking events.

7.2. Shading/Blocking Effects on the Efficiency Loss of the Heliostats

To clarify the role played by shading and blocking in the efficiency loss of the heliostats, the daily amount of shading, blocking, and night events for the same four configurations (Jülich and Protaras, square and rectangular heliostats) and for the three back heliostats (NW, N, and NE) is plotted in Figures 14–17, which is considered a better description of the whole heliostat field. Essentially, the shading and blocking fractions for each hour are obtained, and then the shading and blocking averages for the 08:00–16:00 sampled range are calculated. At 16:00 LCT in Jülich in winter, when altitude < 0, the daily average loss amounts to 0.5/8.0 = 0.0625, as reported in Figures 14 and 15.

The results for all four configurations show that shading is negligible from March to October, as the sun's altitude is high enough, even at 16:00 and 08:00 LCT, to prevent these effects. However, in the winter, shading increases rapidly, particularly at Jülich but also at Protaras. Even in the best case, rectangular heliostats at Protaras, shading loss amounts to 10% around the winter solstice (21st December). Shading decreases sharply on 3rd November and 21st January in Jülich, going in the winter direction, because it becomes night at 16:00 (no shading), and the shading daily average drops.

Unlike shading, blocking is significant, almost constant, from March to October for all four configurations studied here. Blocking is smaller for the central N heliostat, as the reflected rays must point higher to get the target, making them less prone to be intercepted by neighboring heliostats.

As before, the NE heliostat is less efficient than the NW for the four configurations, probably due to the same reasons presented above: the NE heliostat has more difficulty reflecting the rays at 16 than the NW at 8 h. These four graphics seem to suggest that blocking decreases in winter, but this is just a technical effect: when shading occurs, the ray does not reach the mirror, so it is not tested anymore whether the ray could reach the target, and then blocking is not considered. Theoretically, blocking in winter would be significant; however, it is ignored simply because shading occurs first.

An example can be seen in Figures 14 and 15, at Jülich, where the NW heliostat blocking curve suddenly drops when the sun's altitude becomes negative at 16:00, signaling that blocking was occurring at 16:00 at this heliostat when the sun's altitude was still positive. This drop does not occur in the N and NE heliostats, signaling that blocking did not occur at these heliostats. The reason is that the N and NE heliostats were shaded at 16:00, so no blocking was possible, while the NW heliostat cannot be shaded at 16:00, given its westerly position in the field, so blocking can indeed occur.

Finally, it is noted that a heliostat can be shaded and blocked simultaneously: rays in some regions are intercepted before reaching the mirror, and rays in other regions are intercepted after reflection in the mirror. These events are often observed in our simulations.

The graphic representations of the average daily results are very useful to understand the optical phenomena occurring but are inefficient to numerically characterize the whole efficiency of a heliostat field. To produce a quantitative rating for a given heliostat field that can be ranked and compared with other layouts, representative averages for the whole year need to be calculated.

7.3. Average Heliostat Efficiency (AHE)

The DHE average of the 366 days of 2024 (leap year) for each representative heliostat permits defining a yearly heliostat efficiency (YHE):

$$\mathrm{YHE} = \frac{\sum_{i=1}^{366} \mathrm{DHE}_i}{366} \tag{13}$$

Finally, the average of the six representative heliostats allows an average heliostat efficiency (AHE) to be defined for all heliostats, a single figure of merit that is a quantitative, representative, measurement of the efficiency of the geometric layout of the whole heliostat field. As the previous discussions noted, the front-row heliostats have different capabilities (no blocking and little shading) from the other heliostats, so it makes sense to reflect this difference in the average formula used to calculate AHE (see Figure 9):

$$\mathrm{AHE} = \frac{9 \times \frac{\mathrm{YHE}_{SW}+\mathrm{YHE}_{S}+\mathrm{YHE}_{SE}}{3} + (66-9) \times \frac{\mathrm{YHE}_{NW}+\mathrm{YHE}_{N}+\mathrm{YHE}_{NE}}{3}}{66} \tag{14}$$

This single number AHE is convenient because it allows a quick comparison of the relative merits of the various layout configurations. The YHE for the six representative heliostats, plus the corresponding AHE, is reported in Table 2 for the eight configurations studied.

As discussed above, YHE is close to 1.0 for the three front-row heliostats (SW, S, and SE) for all eight configurations (no blocking and residual lateral shading). For the back-row heliostats (NW, N, and NE), YHE decreases substantially, from 0.1 to 0.4, due to significant shading (early morning and late afternoon) and some blocking (midday). As expected, YHE increases 0.05–0.08 when going from Jülich (latitude = 50.9133°) to Protaras (latitude = 35.0125°), as shading decreases. As expected, replacing the flat ground by a 10° slope increases YHE, about 0.07 in Jülich and 0.04 in Protaras. This effect is larger in Jülich, where shading is more significant.

However, the most striking result is the clear superiority of the rectangular heliostats over the square ones, as discussed above. For example, Jülich with flat ground and rectangular heliostats shows a better AHE (0.8213) than Protaras with square heliostats and a 10° slope (0.8121). Replacing square heliostats with rectangular ones (and increasing the north–south distance between heliostats from 1.0 m to 1.9 m to avoid mechanical collisions, as discussed above) increases AHE about 0.13 in Protaras and 0.12–0.14 in Jülich. These improvements are 2–3 times larger than the gains obtained, for example, with the 10° slope.

7.4. Average Total Efficiency (ATE)

The efficiency parameters discussed so far reflect only the heliostat field efficiency as a result of the geometric parameters of the field layout. However, a realistic approach should take into account that the sun radiation flux collected by the heliostats depends decisively upon the altitude of the sun for each hour. That is why this flux is more intense at midday than at 08:00, in the summer than in the winter, and close to the equator than at higher latitudes. A simple, elegant way to take the sun's height into account is to multiply HHE by sin(altitude), assuming that absorption of the sun's radiation by the lower layers of atmosphere is directly proportional to 1—sin(altitude). For example, assuming a maximum flux radiation of 1000 $\mathrm{W/m^2}$, the product 1000 × sin(altitude) results in an effective radiation flux that is maximum at midday, in summer, and closer to the equator. To make this total efficiency more realistic, it can be multiplied by some loss factor, say 0.85, to account for the heliostat reflectivity (including dust, moisture, etc.) plus atmospheric attenuation effects. Using these assumptions, an hourly total efficiency (HTE) for each heliostat can now be defined:

$$\mathrm{HTE} = (1 - S - B) \times \sin(\mathrm{altitude}) \times 0.85 \tag{15}$$

As before, a daily total efficiency (DTE) and a yearly total efficiency (YTE) can now be defined:

$$\mathrm{DTE} = \frac{0.5\mathrm{HTE}_8 + \sum_{i=9}^{15} \mathrm{HTE}_i + 0.5\mathrm{HTE}_{16}}{8} \tag{16}$$

$$\text{YTE} = \frac{\sum_{i=1}^{366} \text{DTE}_i}{366} \tag{17}$$

DTE curves for the eight configurations can be plotted as before, although the sin(altitude) factor tends to predominate, thus hiding other particularities of these curves, making them relatively similar.

Finally, the average of YTE for the six representative heliostats give us a new figure of merit, the average total efficiency (ATE), which should be representative of the whole heliostat field, considering both the geometric layout parameters and the sun's position in the sky:

$$\text{ATE} = \frac{9 \times \frac{\text{YTE}_{SW} + \text{YTE}_{S} + \text{YTE}_{SE}}{3} + (66 - 9) \times \frac{\text{YTE}_{NW} + \text{YTE}_{N} + \text{YTE}_{NE}}{3}}{66} \tag{18}$$

Like AHE, this single ATE number permits an easy comparison of the different layout configurations, but with the advantage of also taking into account the sun's radiation intensity. The YTE for the six representative heliostats, plus the corresponding ATE, is reported in Table 3 for the eight configurations studied.

As expected, ATE values for Jülich (Germany) are much lower (~0.13) than for Protaras (Cyprus), as the sun trajectories are much lower in the first location. These ATE values are much smaller than the AHE values seen before, because the low sun height strongly disadvantages the 08:00–10:00 and 14:00–16:00 periods, particularly at Jülich. The maximum total efficiencies achieved are above 0.5, corresponding to an average radiation flux of 500 W/m^2 for the entire 2024 year, for all days from 8 h to 16 h, assuming that all days are sunny.

Of course, the weather will be cloudy during many of these hours, so no sun radiation (specularly reflected) will reach the target. Extensive research has been reported [28,29] to estimate the distribution of these cloudy days, gathering statistical information—solar radiation data—that plays an important economic role. Assuming that half of the 366 days in 2024 were cloudy (a fairly conservative assumption, to keep this discussion as simple as possible), an average DNI of 250 W/m^2 can be expected for the whole year, from 08:00 to 16:00 LCT, which is still a significant amount of energy. The actual value should be higher, as the cloudy hours are expected to occur mostly in winter, early in the morning, and late in the afternoon, when the sun height is lower and the contribution for ATE is smaller, thus having less of an effect on the whole average.

7.5. Improved Configurations

Comparing simulations with different parameters help us understand how the various aspects are subtlety related, giving us a precious insight to optimize a heliostat field. As an example, we study here the effect of three improvements: (i) increasing the distance between heliostats to 2 m, (ii) increasing the tower height to 20 m, and (iii) increasing the slope to 20°. First, we apply these improvements separately to the worst (Jülich, square, flat) configuration (JSF $\rightarrow$ JSF_1, JSF_2, JSF_3) to compare their efficacy. Finally, the three improvements are combined and applied to the best (Protaras, rectangle, slope) configuration (PRS $\rightarrow$ PRS_{123}) to get a glimpse of the maximum achievable efficiency. AHE and ATE results for these four new configurations are reported in Table 4.

These JSF_1, JSF_2, and JSF_3 results show that AHE improves slightly more when the heliostat distance increases to 2 m, then when the slope rises to 20°, and finally when the tower becomes 20 m high. However, when ATE results are considered, the best result is obtained for the tower improvement, which is better than for the distance improvement and in turn better than the slope improvement. This is because the tower improvement mostly reduces blocking in the 10:00–14:00 period of the most productive hours, while the distance and slope mainly reduce shading in the less productive 08:00–10:00 and 14:00–16:00

intervals. While AHE considers only the geometric efficiency of the heliostat layout, ATE takes into account the sun height at each measuring moment (in our work, hourly from 08:00 to 16:00 LCT), thus providing a better figure of merit to rank the efficiency of the heliostat field to grab energy.

It is interesting to see that AHE for JSF_1 (0.8052), where square heliostats are 2.0 m apart, horizontally and vertically, is still lower than for JRF (0.8213), where rectangular heliostats are separated by 1.0 m horizontally and 1.9 m vertically, reinforcing the conclusion that tall square heliostats block more of the reflected radiation than rectangular heliostats.

The PRS_{123} result is important because it shows approximately the maximum efficiency that can be achieved for this type of heliostat field in the northern hemisphere. AHE is almost equal to 1 (0.9989), so the ATE value measured (0.5498) is about the maximum that can be achieved in Protaras. This is the heliostat field listed in the European Union SFERA-III project [27] with the lowest latitude (+35.0125°), so to obtain better results, it will be necessary to investigate heliostat fields closer to the equator. Assuming a maximum DNI flux of 1000 W/m^2, the value reached for PRS_{123} corresponds to an average flux of 550W/m^2 reaching the target, from 08:00 to 16:00 LCT, from 1st January to 31st December, in 2024 (leap year).

Again, assuming that half of the 366 days in 2024 were cloudy, an average of 275 W/m^2 can be expected for the whole year from 08:00 to 16:00 LCT, an enormous total amount of energy: $275 \times 8 \times 366$ = 805,200 J/m^2. As our simulated heliostat field has 66 mirrors, each of 4 m^2, the total amount of energy collected becomes 805,200 $\times$ 4 $\times$ 66 = 212,572,800 J, the maximum estimated energy collected during the full year of 2024. Results for future years should be very similar, as sun trajectories change very little. For example, on the summer solstice, on 20th June 2025, in Jülich at 08:00 LCT, the altitude and the azimuth are 26″ and 46″ (seconds) larger, respectively, when compared with 2024.

8. Conclusions

(1) Shading is predictably significant at low altitudes, earlier in the morning, and later in the afternoon, but the azimuth also plays a role and is more subtle and difficult to predict.

(2) Blocking occurs at midday and is more significant with square than with rectangular heliostats, because the first are taller and can be slightly more closely packed.

(3) Front-row heliostats suffer no blocking and only lateral shading, while back-row heliostats are much more representative of the whole heliostat field.

(4) The geometric efficiency of a heliostat field can be described by a single number, the average heliostat efficiency (AHE).

(5) The overall efficiency of a heliostat field can also be described by a single number, the average total efficiency (ATE), which depends on the instantaneous sun position. These figures of merit allow easy ranking and comparison of the performance of very different heliostat fields.

(6) To improve ATE, increasing the tower height is more effective (decreasing blocking, when the sun is high) than increasing the distance between heliostats or raising the ground slope to 20° (decreasing shading, when the sun is low).

Author Contributions: J.C.G.P., conceptualization, methodology, software, data curation, validation, and writing—original draft preparation. L.G.R., formal analysis, validation, writing—review and editing, project administration, and funding acquisition. All authors have read and agreed to the published version of the manuscript.

Funding: This work benefited from financial support from the European Union through the SFERA-III project, Grant Agreement No. 823802 (proposal SURPF2101310018-CAHO "Development of Computer Algorithms to Optimize Heliostat Orientation"). The authors would like to thank the

Fundação para a Ciência e a Tecnologia (FCT) for its financial support through the LAETA Base Funding (DOI: 10.54499/UIDB/50022/2020).

Institutional Review Board Statement: Not applicable.

Informed Consent Statement: Not applicable.

Data Availability Statement: The software source code and data supporting the conclusions of this article will be made available by the authors on request.

Acknowledgments: The authors would like to thank the Cyprus Institute for providing access to its installations and the support of its scientific and technical staff in 2022, as part of the European Union SFERA-III project (Grant Agreement No. 823802).

Conflicts of Interest: The authors declare no conflicts of interest.

References

1. World's First Industrial Solar Furnace to Melt Steel Without Fuel or Electricity. Available online: https://energyindustryreview.com/metals-mining/worlds-first-industrial-solar-furnace-to-melt-steel-without-fuel-or-electricity/ (accessed on 21 December 2024).
2. Rodríguez, J.; Cañadas, I.; Zarza, E. PSA vertical axis solar furnace SF5. *Energy Procedia* **2014**, *49*, 1511–1522. [CrossRef]
3. Zayed, M.E.; Zhao, J.; Elsheikh, A.H.; Li, W.; Sadek, S.; Aboelmaaref, M.M. A comprehensive review on Dish/Stirling concentrated solar power systems: Design, optical and geometrical analyses, thermal performance assessment, and applications. *J. Clean. Prod.* **2021**, *283*, 124664. [CrossRef]
4. Singh, H.; Singh, A.; Mishra, R.S.; Pal, A. A Current Review on Linear Fresnel Reflector Technology and Its Applications in Power Plants. In *Recent Advances in Mechanical Engineering (ICRAME 2020)*; Kumar, A., Pal, A., Kachhwaha, S.S., Jain, P.K., Eds.; Springer: Singapore, 2021; pp. 431–440. [CrossRef]
5. Dina, S.F.; Jufrizal, J.; Rambe, S.M.; Limbong, H.P.; Sipahutar, E.P. Design of solar water heater using collector cylindric parabolic and coil heater as absorber at focus point. *E3S Web Conf.* **2021**, *328*, 07016. [CrossRef]
6. Bhattacharjee, R.; Bhattacharjee, S. Performance of inclined heliostat solar field with solar geometrical factors. *Energy Sources Part A Recovery Util. Environ. Eff.* **2020**, *46*, 10450–10472. [CrossRef]
7. Wang, J.; Duan, L.; Yang, Y.; Yang, L. Rapid design of a heliostat field by analytic geometry methods and evaluation of maximum optical efficiency map. *Sol. Energy* **2019**, *180*, 456–467. [CrossRef]
8. Rizvi, A.A.; Yang, D. A detailed account of calculation of shading and blocking factor of a heliostat field. *Renew. Energy* **2022**, *181*, 292–303. [CrossRef]
9. Pidaparthi, A.S.; Duvenhage, D.F.; Hoffmann, J.E. A parametric study of heliostat size for reductions in levelized cost of electricity. In Proceedings of the 4th Southern African Solar Energy Conference (SASEC 2016), Stellenbosch University, Stellenbosch, South Africa, 31 October–2 November 2016. Available online: https://www.researchgate.net/publication/314258829_A_Parametric_Study_of_Heliostat_Size_for_Reductions_in_Levelized_Cost_of_Electricity (accessed on 29 December 2024).
10. Cruz, N.C.; Monterreal, R.; Redondo, J.L.; Fernández-Reche, J.; Enrique, R.; Ortigosa, P.M. Optical characterization of heliostat facets based on computational optimization. *Sol. Energy* **2022**, *248*, 1–15. [CrossRef]
11. Belhomme, B.; Pitz-Paal, R.; Schwarzbözl, P.; Ulmer, S. A new fast ray tracing tool for high-precision simulation of heliostat fields. *J. Sol. Energy Eng.* **2009**, *131*, 031002. [CrossRef]
12. Noone, C.J.; Torrilhon, M.; Mitsos, A. Heliostat field optimization: A new computationally efficient model and biomimetic layout. *Sol. Energy* **2012**, *86*, 792–803. [CrossRef]
13. Bonanos, A.M. Error analysis for concentrated solar collectors. *J. Renew. Sustain. Energy* **2012**, *4*, 063125. [CrossRef]
14. Gonzalo, I.B.; Martínez-Hernández, A.; Romero, M.; Gonzalez-Aguilar, J. Efficient Ray-Tracing Program to Simulate the Optical Performance of Heliostats in Concentrated Solar Power Facilities. In Proceedings of the ISES Solar World Congress 2019, Santiago, Chile, 4–7 November 2019. [CrossRef]
15. Martínez-Hernández, A.; Gonzalo, I.B.; Romero, M.; González-Aguilar, J. Drift analysis in tilt-roll heliostats. *Sol. Energy* **2020**, *211*, 1170–1183. [CrossRef]
16. Deng, H.; Chen, H.; Wang, X. Design of heliostat field based on ray tracing. *Highlights Sci. Eng. Technol.* **2024**, *87*, 10–16. [CrossRef]
17. Teng, Z.; Zhou, H.; Wang, X.; Liu, L.; Jiang, B. Research on optimization design of heliostat field based on ray tracing. *Highlights Sci. Eng. Technol.* **2024**, *104*, 170–179. [CrossRef]
18. Pereira, J.C.G.; Almeida, G.; Rosa, L.G. Computer modelling of heliostat fields by ray-tracing techniques: Simulating the Sun. *Appl. Sci.* **2025**, *15*, 1739. [CrossRef]

19. Pereira, J.C.G.; Fernandes, J.C.; Guerra Rosa, L. Mathematical models for simulation and optimization of high-flux solar furnaces. *Math. Comput. Appl.* **2019**, *24*, 65. [CrossRef]
20. Pereira, J.C.G.; Rodríguez, J.; Fernandes, J.C.; Rosa, L.G. Homogeneous flux distribution in high-flux solar furnaces. *Energies* **2020**, *13*, 433. [CrossRef]
21. Pereira, J.C.G.; Rahmani, K.; Rosa, L.G. Computer Modelling of the Optical Behavior of Homogenizers in High-Flux Solar Furnaces. *Energies* **2021**, *14*, 1828. [CrossRef]
22. Collado, F.J.; Guallar, J. A review of optimized design layouts for solar power tower plants with campo code. *Renew. Sustain. Energy Rev.* **2013**, *20*, 142–154. [CrossRef]
23. Cruz, N.C.; Redondo, J.L.; Berenguel, M.; Álvarez, J.D.; Becerra-Teron, A.; Ortigosa, P.M. High performance computing for the heliostat field layout evaluation. *J. Supercomput.* **2016**, *73*, 259–276. [CrossRef]
24. Zhang, Z.; Zhang, Y.; Xiao, H. A method for calculating the optical efficiency of solar tower heliostats. *Acad. J. Sci. Technol.* **2013**, *8*, 29–33. [CrossRef]
25. Ali, K.; Jifeng, S. Research on modeling simulation and optimal layout of heliostat field optical efficiency for solar power tower plant. *Appl. Sol. Energy* **2023**, *59*, 957–977. [CrossRef]
26. Romero, M.; González-Aguilar, J.; Luque, S. Ultra-modular 500m^2 heliostat field for high flux/high temperature solar-driven processes. *AIP Conf. Proc.* **2017**, *1850*, 030044. [CrossRef]
27. EU SFERA-III Project. Available online: https://sfera3.sollab.eu/access/#infrastructures (accessed on 29 December 2024).
28. Padovan, A.; Col, D.; Sabatelli, V.; Marano, D. DNI estimation procedures for the assessment of solar radiation availability in concentrating systems. *Energy Procedia* **2014**, *57*, 1140–1149. [CrossRef]
29. Abreu, E.F.M. Direct Normal Irradiance and Circumsolar Radiation: Modelling, Measurement and Impact on Concentrating Solar Power. Ph.D. Thesis, Universidade de Évora, Évora, Portugal, 18 October 2023. Available online: http://hdl.handle.net/10174/35737 (accessed on 29 December 2024).